


Green's function theory of spatiotemporally modulated loaded wire surface

Michael Kreiczner  and Yakir Hadad *

School of Electrical Engineering, Ramat-Aviv, Tel Aviv University, Tel Aviv 69978, Israel

 (Received 12 September 2023; revised 13 November 2023; accepted 20 November 2023; published 18 December 2023)

In this paper we explore the two-dimensional Green's function problem above a spatiotemporally modulated loaded wire media. We suggest a spatiotemporal spectral representation to the space-time domain Green's function. Then, we evaluate the spectral representation both by a brute-force numerical integration as well as in a physics-guided fashion by deforming the integration path along the steepest descent path and encircling singular points in the complex spectral plane. The latter approach leads in general to three isolated wave contributions: a refracted ray due to a saddle point contribution, a head-wave-like due to the branch points, and leaky modes that are associated with pole singularities. This way, we identify different wave species that are all subject to a synthetic motion that is effectively caused by the spatiotemporal modulation and give rise to unique nonreciprocal behavior. Lastly, we provide asymptotic closed form expressions for the various waves that comprise the Green's function, as well as conditions under which they contribute.

DOI: [10.1103/PhysRevResearch.5.043256](https://doi.org/10.1103/PhysRevResearch.5.043256)

I. INTRODUCTION

The problem of wave propagation in spatiotemporally modulated media has gained a lot of attention in recent years. One important application that originally pushed forward this research avenue is the possibility to develop magnetless non-reciprocal wave devices in electromagnetics as well as in acoustics [1–21]. These designs are based on the creation of a synthetic sense of motion, that fundamentally enables the breach of time-reversal symmetry with respect to the wave subsystem. While the major part of these efforts has been dedicated to breaking reciprocity in guiding wave structures, some important focus has been also aimed at the violation of reciprocity in scattering and radiation [22–26]. For a comprehensive discussion on the theory and applications of spatiotemporally modulated media the reader is encouraged to read Refs. [27,28].

One major analysis aspect of spatiotemporal metastructures, which has had only a little amount of dedicated research, is the excitation mechanism, with an emphasis on the rigorous analytical Green's function development, and the physical interpretation of the singular and critical points in the complex plane of the spectral variable. In this paper we aim to address this gap. To that end we specifically chose to focus on the excitation problem of an electrically thin spatiotemporally modulated wire metasurface by a localized source located above it. The choice to explore first the excitation dynamics of a metasurface rather than a bulky metamaterial stems from

the substantially greater practicality of the former, as demonstrated, for example in [29–44]. Due to the time variation of the metasurface, a conventional Green's function construction as described for example in [45] for time-harmonic problems is not directly applicable. Instead, here, we perform our analysis for the spatiotemporally modulated wire metasurface problem using a quasifrequency-domain (QFD) approach based on the well-known harmonic balance analysis. Using this approach, in the Green's function spectral construction, we take into account the interharmonic interactions that comprise the temporal dynamics of the metasurface. For the sake of concreteness, we assume that the metasurface consists of an infinite wire array, where each one of the wires is loaded periodically with an inductance and time-varying capacitance that give rise to the spatiotemporal modulation. In order to analyze the metasurface excitation dynamics we take a bottom up approach. We first formulate the excitation of a single time-modulated wire, and later exploit it together with the discrete-dipole approximation [46–51] and the proper Green's function to describe analytically the plane wave scattering from an infinite space-time modulated metasurface. This result is consequently used to construct the Green's function of the problem as a spectral integral. Later, we study the singular and critical points in the complex spectral plane and use them to identify different waves and phenomena in the system.

The paper is organized as follows. For completeness in Sec. II, we provide a brief review on stationary capacitively loaded wire surface. Then, in Sec. III we introduce spatiotemporal modulation to the capacitive loads and provide a thorough mathematical formulation to solve the scattered field by an impinging plane wave from the spatiotemporal metasurface. We augment this analysis in Sec. IV where we develop a synthesis method, for designing the surface for a predetermined ratio between the frequency harmonic to the fundamental frequency, and the angle *bias* from the specular reflection due to the synthetic motion. These required

*hadady@eng.tau.ac.il

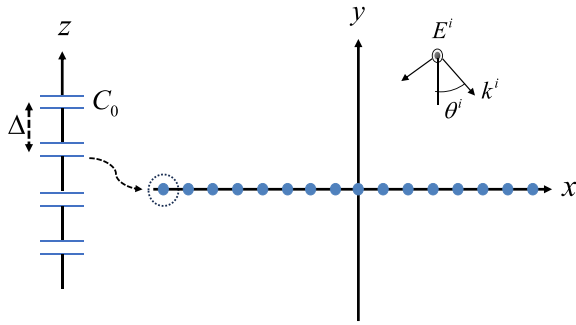


FIG. 1. Stationary loaded wire grid.

properties determine the desired metasurface parameters. Based on the derivations in previous sections, in Sec. V we develop the Green's function of a line source above the metasurface as a spectral integral, and explore the physical interpretation of the singular and critical points in the complex spectral plane through an asymptotic analysis.

II. STATIONARY LOADED WIRE-GRID IMPEDANCE SHEET

In the following sections, we turn to analyze wave phenomena in spatiotemporally modulated loaded wire surfaces. Unavoidably, we will frequently refer to the derivation and the main results of the corresponding, stationary case. Therefore, to make the paper self-contained, in this section, we briefly overview stationary, capacitively loaded wire surfaces. We mainly follow the analysis in [51] for general wire loading and stress the more relevant aspects for the spatiotemporal problem to follow.

Assume that a \hat{z} polarized electromagnetic wave is impinging a loaded wire surface as shown in Fig. 1. We assume that the wires are surrounded by a vacuum with permittivity and permeability denoted by ϵ_0 and μ_0 , respectively. The grid points are given by $\vec{R}_l = la\hat{x}$, where a is the unit-cell dimension, and l denotes its index. The induced current on each of the wires is given by $\vec{I} = \alpha \vec{E}^{\text{loc}}$ where \vec{E}^{loc} is the local electric field, namely, the electric field at the wire location but in the absence of the wire itself, and α is the wire susceptibility. A \hat{z} polarized incident plane wave arrives from the positive y axis,

$$\vec{E}^{\text{inc}} = \hat{z} E^i e^{-j\vec{k}^i \cdot \vec{r}}, \quad (1)$$

where the impinging wave wavevector $\vec{k}^i = -k \cos \theta^i \hat{y} + k \sin \theta^i \hat{x}$. If the wires are periodically loaded by lumped impedance Z_L , with periodicity $\Delta \ll \lambda$, the inverse susceptibility satisfies [51]

$$\alpha^{-1}(\omega) = \alpha_0^{-1}(\omega) + \frac{Z_L}{\Delta} \quad (2)$$

where $\alpha_0^{-1}(\omega) = \frac{\eta k}{4} H_0^{(2)}(kr_0)$. For example, for serial loading of lumped capacitors $Z_L/\Delta = 1/(j\omega C_0)$. Here $\eta = 120\pi \Omega$, and $k = \omega/c$ are the free space impedance and wavenumber, respectively, ω is the radial frequency, c is the speed of light in vacuum, r_0 is the wire radius, and $H_0^{(2)}$ denotes the zeroth-order Hankel function of the second type. It should be emphasized that there are additional, more accurate, ways

to describe the periodic wire loading [52,53]. However, since we aim mainly at the fundamental physical effects, we limit this paper to the relatively simple and intuitive approximation in Eq. (2), which has been demonstrated to be effective and sufficiently accurate through full-wave simulations and experiments in various works such as [54]. In light of the lattice periodicity, the Floquet-Bloch wave solution is expected,

$$I_l = A e^{-jk_x^i l a} \quad (3)$$

where k_x^i is the \hat{x} component of the incident plane wave. Then, the induced current is found by solving the equation for the boundary conditions

$$\alpha_0^{-1} I_l = E^{\text{inc}}(\vec{r}_l) + \sum_{l' \neq l} G(\vec{r}_l, \vec{r}_{l'}) I_{l'} \quad (4)$$

where $G(\vec{r}_l, \vec{r}_{l'}) = \frac{-\eta k}{4} H_0^{(2)}(k|\vec{r}_l - \vec{r}_{l'}|)$. We can now calculate the sum in Eq. (4)

$$\sum_{l' \neq l} G(|\vec{r}_l - \vec{r}_{l'}|) I_{l'} = A e^{-jk_x^i a l} \left(-\frac{\eta k}{2} \right) S \quad (5)$$

with

$$S = \sum_{m=1}^{\infty} H_0^{(2)}(kam) \cos(k_x^i am). \quad (6)$$

Since our structure is periodic and the impinging wave is a plane wave, the currents on the different wires are identical in their amplitude and vary only in a linear phase factor as given in Eq. (3). Therefore, with no loss of generality, we may write the expression for the current on the wire $l = 0$.

$$I_0 = \frac{E^i}{\left(\frac{\eta k}{4} H_0^{(2)}(kr_0) + \frac{1}{j\omega C_0 \Delta} \right) + \frac{\eta k}{2} S}. \quad (7)$$

Up to this point, the derivation is exact. Now, we will focus on the dense grid approximation, which will be of interest in the following sections where we explore Green's function above a space-time varying dense grid. In the dense grid approximation, high-order Floquet modes are evanescent, which implies the mathematical condition $a \ll \frac{\lambda}{2}$ for all the relevant harmonics that non-negligibly excited (for weak modulation these are typically ± 1). Under the described conditions, we may define the cell-averaged current $J_s = \frac{I_0}{a} \hat{z}$, and approximate by (see Appendix A)

$$\vec{J}(x) \approx \frac{\frac{E^i}{a} e^{-jk_x^i x \hat{z}}}{\frac{j\eta k}{2\pi} \left(\ln \frac{a}{2\pi r} \right) + \frac{1}{j\omega C_0 \Delta} + \frac{\eta k}{2a\sqrt{k^2 - (k_x^i)^2}}}. \quad (8)$$

The relation between the average current and the tangential component of the scattered magnetic field is $\hat{y} \times \vec{H}_t^{\text{scat}}(x, y = 0^+) = -\frac{J}{2} \hat{x}$. For the case of TE wave, the impedance of the scattered wave is given by $\underline{Z} = Z_{TE}^{\text{scat}} \frac{\hat{y} \times \vec{k}_x^{\text{inc}} \cdot \hat{y} \times \vec{k}_x^{\text{inc}}}{(k_x^{\text{inc}})^2}$ with $Z_{TE}^{\text{scat}} = \frac{\eta}{\sqrt{1 - \frac{(k_x^i)^2}{k^2}}}$. The averaged scattered electric field satisfies

$$\vec{E}_t^{\text{scat}}(x, y = 0^+) = -\frac{\hat{z} E^i e^{-jk_x^i x} Z_{TE}^{\text{scat}}}{\frac{j\eta k}{2\pi} \left(\ln \frac{a}{2\pi r} \right) + \frac{1}{j\omega C_0 \Delta} + \frac{Z_{TE}^{\text{scat}}}{2a}}. \quad (9)$$

With the total field and the surface current, we can write the effective impedance of the surface

$$Z_g = \frac{E_{tot}}{J_s} \approx j \left(\frac{\eta k a}{2\pi} \ln \frac{a}{2\pi r_0} - \frac{a}{\omega c \Delta} \right) \quad (10)$$

where $\vec{E}_t^{tot} = \vec{E}^{inc} + \vec{E}^{scat}$.

III. WIRE SURFACE WITH SPATIOTEMPORALLY MODULATED CAPACITIVE LOADING

A. General formulation and harmonic balance

Our goal in this paper is to explore the 2D Green's function problem above a spatiotemporally modulated wire layer, as illustrated in Fig. 2. In this section we borrow the analytical modeling previously developed in [10] for a time-modulated wire, as well as for the interwire interaction, as our building blocks. Using these building blocks, we first begin with the scattering problem due to a single monochromatic plane wave incidence. This will later be used to construct the spectral solution for a localized source. Our analysis is based on the concept of harmonic balance, which can be regarded as a quasifrequency domain (QFD) technique. The stationary capacitive loading of the previous section is now modulated in time,

$$C(t) = C_0 + \delta C(\cos \Omega t - \varphi), \quad m = \frac{\delta C}{C_0} \ll 1. \quad (11)$$

This time-variant capacitance leads to spatiotemporally modulation, with Ω representing the temporal modulation. The spatial modulation can be achieved when demanding linear phase accumulation along the metasurface, i.e., $\varphi_l = l\Delta\varphi$. Without loss of generality, we choose $\Delta\varphi > 0$. In light of the harmonic time modulation the local field has the following frequency dependence:

$$E^{loc}(\omega) = \sum_{n=-\infty}^{\infty} E_n^{loc} \delta(\omega - \omega_n) \quad (12)$$

with $\omega_n = \omega_0 + n\Omega$, and $\delta(\cdot)$ denotes Dirac's delta. Then, for the current we have

$$I(\omega) = \sum_{n=-\infty}^{\infty} I_n \delta(\omega - \omega_n). \quad (13)$$

Here, E_n^{loc} and I_n denote the n th harmonic complex amplitude of the local field and of the induced current on the wires, respectively. By balancing the coefficients of equal harmonics

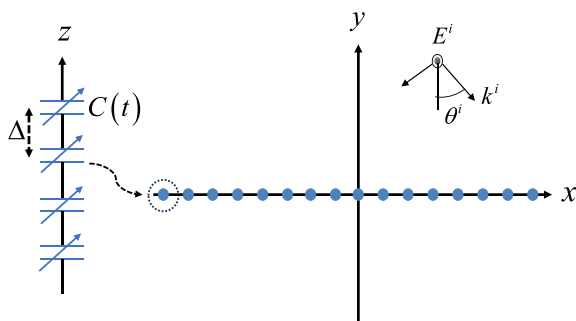


FIG. 2. Spatiotemporal Loaded wire grid.

we find that for a single wire,

$$E_n^{loc} = \left[\alpha_0^{-1}(\omega_n) + \frac{1}{j\omega_n \tilde{C}} \right] I_n - \frac{m}{2} \left[\frac{e^{-j\varphi}}{j\omega_{n-1} \tilde{C}} I_{n-1} + \frac{e^{j\varphi}}{j\omega_{n+1} \tilde{C}} I_{n+1} \right], \quad (14)$$

where $\tilde{C} = C_0 \Delta$. We can now generalize the method of the previous section of the unperturbed stationary loads. The incident wave is assumed with a single frequency ω_0 . Since the intermodulation will give rise to scattered fields at multiple frequencies ω_n , we use the representation in Eqs. (12) and (13). Due to Floquet-Bloch theorem, the current will be in the form

$$I_l(\omega) = \sum_{n=-\infty}^{\infty} A_n e^{-jl(k_x^i a + n\Delta\varphi)} \delta(\omega - \omega_n). \quad (15)$$

Like in the LTI, stationary case, we can write Eq. (15) also for the reference wire at $x = 0$. The effective incident field for the wire at $x = 0$ will be E^{loc} , and is composed of the impinging plane wave at ω_0 , and the field radiated by the rest of the wires. The latter contains multiple frequencies,

$$E^{loc} = E^i \delta(\omega - \omega_0) + \sum_{l \neq 0} \sum_{n=-\infty}^{\infty} G_n(|l'a|) A_n e^{-j(k_x^i a + n\Delta\varphi)} \delta(\omega - \omega_n), \quad (16)$$

where $G_n(|\vec{r} - \vec{r}'|) = \frac{-\eta k_n}{4} H_0^{(2)}(k_n |\vec{r} - \vec{r}'|)$ denoting the two dimensional Green's function at the n th harmonic for a source located at \vec{r}' . The dense grid condition is now requiring ($k_n a \ll 1$), i.e., the grid is dense compared to the wavelengths of the high harmonics (which are yet assumed significant enough not to be neglected). Now, we need to calculate the expressions $\{A_n\}$, by comparing the coefficients of the delta functions. As opposed to the stationary-loaded-wire-medium case, where the effective current may be analytically expressed using Eq. (8), for the spatiotemporally modulated case, the interaction between the different temporal-frequency harmonics should be included,

$$\frac{-m}{2j\omega_{n-1} \tilde{C}} A_{n-1} + \left[\gamma_0 \omega_n + \frac{1}{j\omega_n \tilde{C}} + \frac{1}{2} \eta k_n S_n \right] A_n + \frac{-m}{2j\omega_{n+1} \tilde{C}} A_{n+1} = E^i \delta_{0n}. \quad (17)$$

Here, δ_{0n} is the delta of Kronecker, and $S_n = \sum_{m=1}^{\infty} H_0^{(2)}(k_n a m) \cos(k_x^i a + n\Delta\varphi) m$. For a dense grid S_n can be approximated with

$$S_n \approx \frac{1}{a\sqrt{k_n^2 - (k_x^i + \frac{n\Delta\varphi}{a})^2}} - \frac{1}{2} + \frac{j}{\pi} \left[\ln \frac{k_n a}{4\pi} + \gamma \right]. \quad (18)$$

The approximate recursive relation can now be represented using a tridiagonal matrix of infinite rank,

$$\underline{\underline{U}} \underline{\underline{A}} = \underline{\underline{E}}^i, \quad (19)$$

where \underline{U} , \underline{A} , and \underline{E}^i are correspondingly given below

$$\begin{bmatrix} \ddots & \ddots & 0 & 0 & & & & & & \\ \ddots & b_{-2} & c_{-2} & 0 & 0 & & & & & \\ 0 & a_{-1} & b_{-1} & c_{-1} & 0 & 0 & & & & \\ 0 & 0 & a_0 & b_0 & c_0 & 0 & 0 & & & \\ & & 0 & 0 & a_1 & b_1 & c_1 & 0 & & \\ & & & 0 & 0 & a_2 & b_2 & \ddots & & \\ & & & & 0 & 0 & \ddots & \ddots & & \end{bmatrix} \begin{bmatrix} \vdots \\ A_{-2} \\ A_{-1} \\ A_0 \\ A_1 \\ A_2 \\ \vdots \end{bmatrix} = \begin{bmatrix} \vdots \\ 0 \\ 0 \\ E^i \\ 0 \\ 0 \\ \vdots \end{bmatrix}. \quad (20)$$

The matrix entries a_n, b_n, c_n are

$$a_n = -\frac{m}{2j\omega_{n-1}\tilde{C}}, \quad (21a)$$

$$b_n = \frac{\eta k_n}{2a\sqrt{k_n^2 - k_{n,x}^2}} + j\left(\omega_n \tilde{L}_w - \frac{1}{\omega_n \tilde{C}}\right), \quad (21b)$$

$$c_n = -\frac{m}{2j\omega_{n+1}\tilde{C}}, \quad (21c)$$

where we defined the effective \hat{x} component of the wave number for the n th harmonic with $k_{n,x} = k_x^i + \frac{n\Delta\varphi}{a}$, and the wire intrinsic inductance with $\tilde{L}_w = \frac{\eta}{2\pi c} \ln \frac{a}{2\pi r_0}$. We assume that for large enough N , the currents of harmonic $N + 1$ $A_{-(N+1)}, A_{N+1}$, and above, are negligible. In this case, the infinite matrix can be approximated by a finite $(2N + 1) \times (2N + 1)$ square matrix

$$\underline{U}^{(N)} = \begin{bmatrix} b_{-N} & c_{-N} & 0 & & & & & & & \\ a_{-N+1} & \ddots & \ddots & 0 & & & & & & \\ 0 & \ddots & b_{-2} & c_{-2} & 0 & & & & & \\ & & 0 & a_{-1} & b_{-1} & c_{-1} & 0 & & & \\ & & & 0 & a_0 & b_0 & c_0 & 0 & & \\ & & & & 0 & a_1 & b_1 & c_1 & 0 & \\ & & & & & 0 & a_2 & b_2 & \ddots & 0 \\ & & & & & & 0 & \ddots & \ddots & c_{N-1} \\ & & & & & & & 0 & a_N & b_N \end{bmatrix}. \quad (22)$$

B. Excitation and energy transfer between harmonics

In the preceding section, we have presented the formulation of the excitation problem by a plane wave interacting with a space-time modulated wire grating. In the subsequent discussion, we will delve into the examination of the reflection and transmission dynamics, followed by the development of the Green's function by a 2D current line source. In this section, we shall analyze the power exchange between the spatiotemporal harmonics as dictated by the modulation parameters and the geometry. To initiate this analysis, we introduce a series inductance L_0 , which serves the purpose of obviating the necessity of employing wires with excessively small and impractical radius r_0 , as depicted in Fig. 3. We define the effective resistance and the effective inductance with

$$\tilde{R}_n(\omega) = \frac{\eta k_n}{2a\sqrt{k_n^2 - (k_{n,x})^2}}, \quad (23a)$$

$$\tilde{L} = \frac{L}{\Delta} + \tilde{L}_w. \quad (23b)$$

Clearly, this definition is only valid when \tilde{R}_n is a positive real value, i.e., $k_n > k_{n,x}$. When $k_n < k_{n,x}$ it means that there are no propagating plane waves that are reflected by the wire surface,

instead the spectrum is evanescent. This condition limits us to slow synthetic motion effect $\Delta\varphi < \frac{k_n - k_0}{n} a$. In that case, b_n can be now written with

$$b_n = \tilde{R}_n + j\tilde{X}(\omega) \quad (24)$$

where $\tilde{X}(\omega) = \omega\tilde{L} - \frac{1}{\omega\tilde{C}}$. In order to be able to approximate the wire surface behavior by that of an RLC circuit, we need to approximate the constant resistance $\tilde{R}_n(\frac{\delta\omega}{\omega^0}) \approx \text{const}$. The quality factor Q_n of each harmonic b_n can be defined as $\tilde{Q}_n = \frac{1}{\tilde{R}_n} \sqrt{\frac{\tilde{L}}{\tilde{C}}}$. In order to achieve a good separation between the harmonics and an effective excitation, we focus on the case of a large quality factor $\tilde{Q}_n \gg 1$. The analysis will be near a desired frequency ω^0 , such that $\omega_0 = \omega^0 + \delta\omega$. Let us define with n_r the harmonic n , which has a resonance behavior, i.e., $\omega^0(1 + n_r \frac{\Omega}{\omega^0}) = \frac{1}{\sqrt{\tilde{L}\tilde{C}}}$. Suppose we aim to illuminate the surface with an impinging wave at ω^0 , and get a strong response at the center frequency with harmonic number n_r , then the inductance needs to be set,

$$\tilde{L} = \frac{1}{\tilde{C}(1 + n_r \frac{\Omega}{\omega^0})^2}. \quad (25)$$

For a given \tilde{C} , we can now calculate the quality factor for each harmonic. Let us define the ‘‘dominance parameter’’ D_n with

$D_n = \frac{a_n(\frac{\delta\omega}{\omega^0}=0)}{b_n(\frac{\delta\omega}{\omega^0}=0)}$. In the next section, we use this parameter to design a wire grid with desired specifications. We get

$$D_n = \frac{-\frac{m}{2j\omega^0(1+(n-1)\frac{\Omega}{\omega^0})\tilde{C}}}{\tilde{R}_n + j\left[\omega^0(1+n\frac{\Omega}{\omega^0})\tilde{L} - \frac{1}{\omega^0(1+n\frac{\Omega}{\omega^0})\tilde{C}}\right]}. \quad (26)$$

For the resonant harmonic, we can use $Q_n = \frac{1}{\omega^0(1+n\frac{\Omega}{\omega^0})\tilde{R}_n\tilde{C}}$ and get the approximate expression

$$D_{n_r} \approx -\frac{m\tilde{Q}_{n_r}}{2j}\left(\frac{1+n_r\frac{\Omega}{\omega^0}}{1+(n_r-1)\frac{\Omega}{\omega^0}}\right). \quad (27)$$

We can see that in order to achieve large D_{n_r} , we must demand $Q_{n_r} \gg \frac{1}{m}$. In that case, the bandwidth satisfies $BW_{n_r} \approx \omega^0(1+n_r\frac{\Omega}{\omega^0})/Q_{n_r}$. Let us now approximate D_n for the case of $n \neq n_r$. As mentioned before, we assume high quality factor for the resonance, in order to achieve good separation. Also we use $O(\frac{\tilde{R}_n}{\tilde{R}_{n_r}}) = 1$, since in our case we need to demand $k_n > k_{n,x}$ in order to reflect a propagating plane wave,

$$D_{n \neq n_r} \approx \frac{\frac{m}{2(1+(n-1)\frac{\Omega}{\omega^0})}}{\frac{(1+n\frac{\Omega}{\omega^0})}{(1+n_r\frac{\Omega}{\omega^0})^2} - \frac{1}{(1+n\frac{\Omega}{\omega^0})}}. \quad (28)$$

We note that in our approximation D_{n_r} is purely imaginary, and $D_{n \neq n_r}$ is purely real. Clearly, for a good separation between the harmonics we need to demand $|D_{n \neq n_r}| \ll 1$, which leads to $|\frac{a_i c_j}{b_i b_j}| \ll 1$ for $i, j \neq n_r$ and $|\frac{a_i c_j}{b_i b_j}| \gg 1$ for i or $j = n_r$. With Cramer's rule [55] we can approximate the currents

$$A_n = \frac{|U_{=n}^{(N)}|}{|U_{=0}^{(N)}|} \quad (29)$$

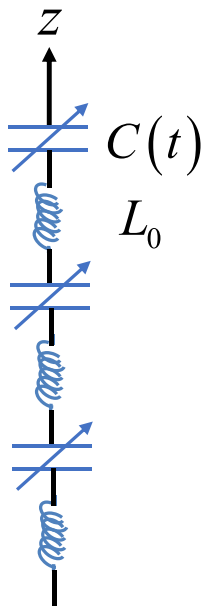


FIG. 3. Wire with added constant inductance L_0 .

where $\underline{U}_{=n}^{(N)}$ is the matrix, in which the vector E^i replaces the column n (see Appendix B). For a tridiagonal matrix, the determinant satisfies the recurrence relation [55]

$$\begin{aligned} f_n &= b_n f_{n-1} - a_n c_{n-1} f_{n-2}, \\ f_{-N} &= |b_{-N}|, \\ f_{-(N+1)} &= 1, \\ f_{-(N+2)} &= 0. \end{aligned} \quad (30)$$

For high quality factor, the denominator of Eq. (29) can be approximated as

$$|\underline{U}_{=n}^{(N)}| \approx \left(1 - \frac{a_n c_{n-1}}{b_n b_{n-1}} - \frac{a_{n+1} c_n}{b_{n+1} b_n}\right) \prod_{i=-N}^N b_i \quad (31)$$

while for to the nominator of Eq. (29), we approximate for $n = n_r > 0$,

$$|\underline{U}_{=n_r}^{(N)}| \approx (-1)^{n_r} E^i \prod_{i=-N}^{-1} b_i \prod_{i=1}^{n_r} a_i \prod_{i=n_r+1}^N b_i. \quad (32)$$

(For detailed derivation, see Appendix B). It is of interest to calculate the current for the fundamental harmonic, i.e., for $n = 0$. The expression is different for the case of $n_r = 1$ and for $n_r > 1$ (we focus on the case of resonance at positive harmonic number),

$$|\underline{U}_{=0}^{(N)}| \approx \begin{cases} \frac{E^i}{b_0} \left(1 - \frac{a_{n_r} c_{n_r-1}}{b_{n_r} b_{n_r-1}} - \frac{a_{n_r+1} c_{n_r}}{b_{n_r+1} b_{n_r}}\right) \prod_{n=-N}^N b_n & n_r \geq 2 \\ \frac{E^i}{b_0} \left(1 - \frac{a_{n_r+1} c_{n_r}}{b_{n_r+1} b_{n_r}}\right) \prod_{n=-N}^N b_n & n_r = 1 \end{cases}. \quad (33)$$

And we get the current for the resonance harmonic and the fundamental frequency,

$$\begin{aligned} A_{n_r} &\approx \frac{(-1)^{n_r} E^i \prod_{n=1}^{n_r} \frac{a_n}{b_n}}{b_0 \left(1 - \frac{a_{n_r} c_{n_r-1}}{b_{n_r} b_{n_r-1}} - \frac{a_{n_r+1} c_{n_r}}{b_{n_r+1} b_{n_r}}\right)}, \\ A_0 &\approx \begin{cases} \frac{E^i}{b_0} \left(1 - \frac{a_2 c_1}{b_2 b_1}\right) & n_r = 1 \\ \frac{E^i}{b_0} & n_r \geq 2 \end{cases}. \end{aligned} \quad (34)$$

In order to qualitatively describe the power exchange between different temporal harmonics we define the interharmonic transfer ratio by

$$T_{n_r} = \left|\frac{A_{n_r}}{A_0}\right|^2. \quad (36)$$

The transfer ratio allows us to design and calculate the grid parameters, which is to be detailed in the next section. It is important to note that this value represents the ratio between the energy of a plane wave scattered at the resonant harmonic and the energy scattered at the fundamental frequency. These energies both are smaller than the incident wave energy, since in order to achieve the high quality factor, we needed to design a surface that has an unmatched impedance, which leads to the transparent-like behavior of the surface. The larger $|n_r|$, the

stronger this phenomenon gets. Specifically, we can express T_{n_r} for any n_r by

$$T_{n_r} = \begin{cases} \left| \frac{\frac{a_1}{b_1}}{1 - \frac{a_2 c_1}{b_2 b_1}} \right|^2 & n_r = 1 \\ \left| \frac{\prod_{n=1}^{n_r} \frac{a_n}{b_n}}{1 - \frac{a_{n_r} c_{n_r-1}}{b_{n_r} b_{n_r-1}} - \frac{a_{n_r+1} c_{n_r}}{b_{n_r+1} b_{n_r}}} \right|^2 & n_r \geq 2 \end{cases}. \quad (37)$$

C. The scattered plane wave

In this section, we shall use the induced current on the dense wire grid in order to express analytically the reflected and transmitted fields. Following the usual approach [see Eq. (8) and discussion there], here we begin by averaging the current on the dense wire grid. We use the expression in Eq. (13),

$$\vec{J}_s = \hat{z} \sum_{n=-\infty}^{\infty} J_{s,n} \delta(\omega - \omega_n), \quad (38)$$

where

$$J_{s,n} = \frac{1}{a} A_n e^{-jk_{n,x}x}. \quad (39)$$

With the synthetic motion effect, we can also define the wave vector of the n th harmonic of the scattered field,

$$\vec{k}_n = \hat{x} \left(k^i + \frac{n\Delta\varphi}{a} \right) + \hat{y} \sqrt{k_n^2 - \left(k_x^i + \frac{n\Delta\varphi}{a} \right)^2}. \quad (40)$$

Then, the corresponding reflection angle reads $\sin \theta_n^r = k_{n,x}^i / k_n$. The scattered tangential magnetic field for the n th harmonic satisfies $\hat{y} \times \vec{H}_{n,t}^{\text{scat}}(y = 0^+) = \vec{J}_{s,n} / 2$. The scattered electric field is calculated similarly to that of a stationary surface. However, we note that the synthetic motion due to the spatiotemporal modulation of the wires implies effectively a different incident wave for each excited harmonic, with a different angle of arrival. The effective incident wave, for the low and high harmonics, will be derived with our definition of \vec{k}_n . We can now calculate the scattered field from the grid,

$$\vec{E}_n^{\text{scat}}(y = 0^+) = -Z_{TE,n}^{\text{scat}} \frac{\hat{z} A_n e^{-jk_{n,x}x}}{2a} \quad (41)$$

where $Z_{TE,n}^{\text{scat}} = \eta / \sqrt{1 - k_{n,x}^2 / k_n^2}$. In order to obtain the total field, we need to add the incident electric field to the scattered electric field. We can also substitute the expressions for the TE impedance. This leads to the total electric field for the n th harmonic,

$$E_n^{\text{tot}}(y = 0^+) = \left(\delta_{0n} E^i - \frac{\eta k_n A_n}{2a \sqrt{k_n^2 - k_{n,x}^2}} \right) e^{-jk_{n,x}x}. \quad (42)$$

The surface impedance of the spatiotemporally modulated wire grid is the ratio between the total field and the current. The surface impedance takes the form of a diagonal matrix whose elements are given by

$$Z_n = \frac{a}{\tilde{A}_n} \left(\delta_{0n} - \frac{\eta k_n \tilde{A}_n}{2a \sqrt{k_n^2 - k_{n,x}^2}} \right), \quad (43)$$

where \tilde{A}_n can be thought of as the impedance that relates the n th harmonic of the current of the reference wire, and the impinging electric field. Namely, $\tilde{A}_n = A_n / E_i$.

IV. SYNTHESIS OF SPACE-TIME MODULATED METASURFACE

Let us now use the dominance definition, to calculate the current at the center frequency of the resonance harmonic $A_{n_r}(\frac{\delta\omega}{\omega^0} = 0)$. We start with a design goal for a certain energy transfer ratio from the fundamental harmonic T_{n_r} . We use the approximations for the dominance D_n , for $n = n_r$ (27) and $n \neq n_r$ (28). Since the approximations for T_{n_r} in (37) is different for $n_r = 1$ and $n_r > 1$, the analysis is split accordingly. We start with $n_r = 1$. We use $\frac{c_n}{a_n} = \frac{1+(n-1)\frac{\Omega}{\omega^0}}{1+(n+1)\frac{\Omega}{\omega^0}}$, and the expressions for D_n . The fact that D_1 is purely imaginary and D_2 is purely real (for large quality factors) can be used,

$$T_{n_r=1} \left(\frac{\delta\omega}{\omega^0} = 0 \right) = \frac{|D_1|^2}{1 + |D_2|^2 |D_1|^2 \frac{1}{(1+2\frac{\Omega}{\omega^0})^2}}. \quad (44)$$

D_1 can now be calculated, and after that the needed quality factor Q_{n_r} . We define $T_1 = T_{n_r=1}(\frac{\delta\omega}{\omega^0})$. The expression for D_1 can be written as

$$|D_1| = \sqrt{\frac{T_1}{1 - |D_2|^2 \frac{1}{(1+2\frac{\Omega}{\omega^0})^2} T_1}}. \quad (45)$$

And with Eq. (27), we calculate Q_1 as

$$\tilde{Q}_1 = \frac{2|D_1|}{m(1 + \frac{\Omega}{\omega^0})}. \quad (46)$$

Let us now repeat the analysis with $n_r > 1$. Here we can write

$$T_{n_r} \left(\frac{\delta\omega}{\omega^0} = 0 \right) = \frac{|D_{n_r}|^2 \prod_{n=1}^{n_r-1} |D_n|^2}{1 + |D_{n_r}|^2 \left| D_{n_r-1} \frac{1+(n_r-2)\frac{\Omega}{\omega^0}}{1+n_r\frac{\Omega}{\omega^0}} + D_{n_r+1} \frac{1+(n_r-1)\frac{\Omega}{\omega^0}}{1+(n_r+1)\frac{\Omega}{\omega^0}} \right|^2}. \quad (47)$$

When again we used the fact that D_{n_r} is purely imaginary, and $D_{n \neq n_r}$ is approximately purely real. We get D_{n_r} ,

$$|D_{n_r}| = \left[\frac{T_{n_r}}{\prod_{n=1}^{n_r-1} |D_n|^2 - \left| D_{n_r-1} \frac{1+(n_r-2)\frac{\Omega}{\omega^0}}{1+n_r\frac{\Omega}{\omega^0}} + D_{n_r+1} \frac{1+(n_r-1)\frac{\Omega}{\omega^0}}{1+(n_r+1)\frac{\Omega}{\omega^0}} \right|^2 T_{n_r}} \right]^{\frac{1}{2}}. \quad (48)$$

And with Eq. (27), we calculate Q_{n_r} as

$$\tilde{Q}_{n_r} = \frac{2|D_{n_r}|}{m} \frac{1 + (n_r - 1) \frac{\Omega}{\omega^0}}{1 + n_r \frac{\Omega}{\omega^0}}. \quad (49)$$

We wish to conclude this section with a numerical example. Let us explore two cases that only differ in their energy

TABLE I. The two different cases, which differ from each other only with the transfer ratio.

	T_{nr} [dB]	θ^i	$\frac{\Omega}{\omega^0}$	$\Delta\varphi$	m
Case I	12	$\frac{\pi}{10}$	0.3	$\frac{\pi}{20}$	0.25
Case II	6	$\frac{\pi}{10}$	0.3	$\frac{\pi}{20}$	0.25

transfer ratio T_{nr} . The relevant parameters for these two cases are provided in Table I. In Case I, we take a relatively high transfer ratio $T_{nr} = 12$ dB, while in Case II, we have a relatively small transfer ratio $T_{nr} = 6$ dB. The parameters common to both cases are $a = 0.1\lambda^0$, $m = 0.25$, and $\theta^i = \pi/10$. The quality factors for the high transfer ratio are $Q_1 = 36$ ($n_r = 1$) and $Q_2 = 60$ ($n_r = 2$), whereas for the low transfer ratio, we have $Q_1 = 13$ ($n_r = 1$) and $Q_2 = 28$ ($n_r = 2$). Accurate solutions are obtained by directly inverting the matrix \underline{U} , while approximate solutions are derived using the method presented earlier. The excited currents in these cases, normalized by the induced current on the corresponding stationary metasurface are shown in Fig. 4. The continuous lines represent the approximate solutions, which show good agreement with the discrete circles representing the more accurate solutions obtained by matrix inversion. For Case I, at $n_r = 1$ in Fig. 4(a), we obtain $\tilde{C} = 3.1 \times 10^{-16}$ Fm and $\tilde{L} = 4.3 \times 10^{-5}$ H/m. For $n_r = 2$, in Fig. 4(b), we have $\tilde{C} = 2.3 \times 10^{-16}$ Fm and $\tilde{L} = 4.3 \times 10^{-5}$ H/m. For Case II, at $n_r = 1$ in Fig. 4(c), we find $\tilde{C} = 3.1 \times 10^{-15}$ Fm and $\tilde{L} = 1.1 \times 10^{-5}$ H/m. For $n_r = 2$, in Fig. 4(d), we obtain $\tilde{C} = 4.9 \times 10^{-16}$ Fm and $\tilde{L} = 2 \times 10^{-5}$ H/m. Figure 5 illustrates the transfer ratio calculated numerically for both cases, demonstrating our ability to select analytically the wire loading required to achieve certain design goals.

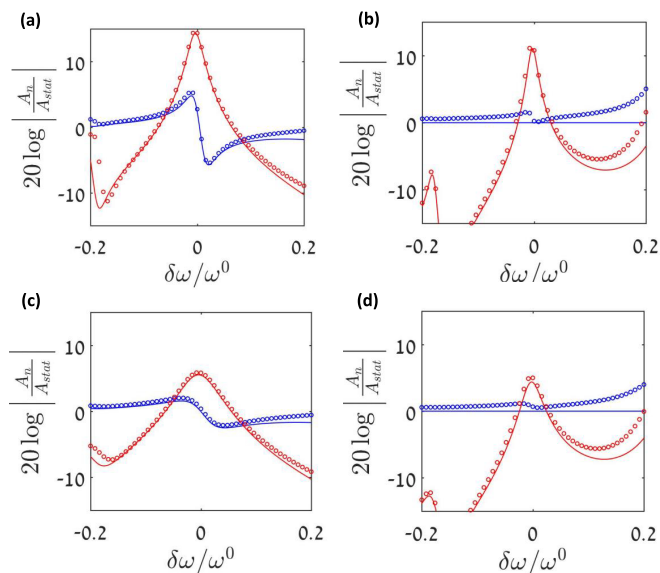


FIG. 4. Currents for the fundamental harmonic (blue) and the resonance harmonic (red), normalized with the current of the stationary media. Continuous line represents approximate calculation and circles represents the exact solution (a) $T = 12$ dB, $n_r = 1$; (b) $T = 12$ dB, $n_r = 2$; (c) $T = 6$ dB, $n_r = 1$; (d) $T = 6$ dB, $n_r = 2$.

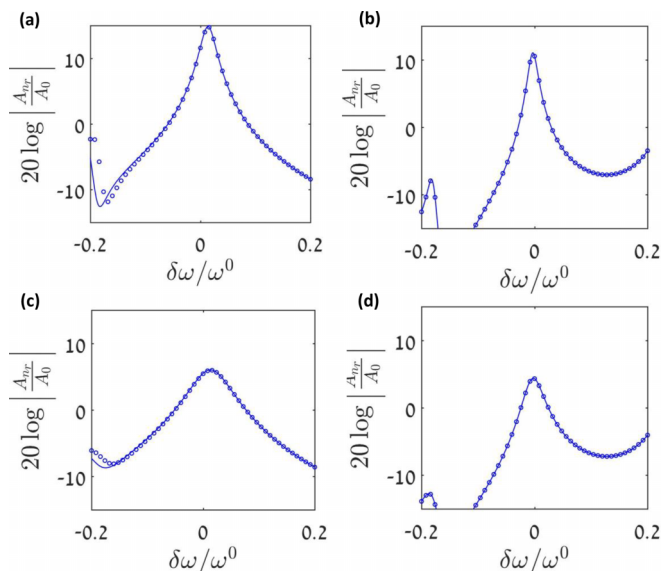


FIG. 5. Ratio between the currents of the resonance harmonic to the fundamental frequency. The continuous line represents approximate calculation and the circles represent the exact solution. (a) $T = 12$ dB, $n_r = 1$; (b) $T = 12$ dB, $n_r = 2$; (c) $T = 6$ dB, $n_r = 1$; (d) $T = 6$ dB, $n_r = 2$.

V. EXCITATION BY A LOCALIZED SOURCE—THE 2D GREEN'S FUNCTION

In this section, our objective is to calculate the 2D Green's function above a spatiotemporal modulated wire grid and derive a spectral integral representation for it. Figure 6 illustrates the problem setup. To accomplish this, we first decompose the line source field into a spectrum of plane waves. Subsequently, each of these plane waves interacts with the spatiotemporal modulated wire grid using the theory derived in previous sections. To simplify our analysis and obtain relatively concise expressions, we focus on the case of high quality factor for the resonant harmonic. Lastly, we asymptotically evaluate the resulting spectral integral and extract insights regarding the different wave creatures propagating in this particular spatiotemporally modulated platform.

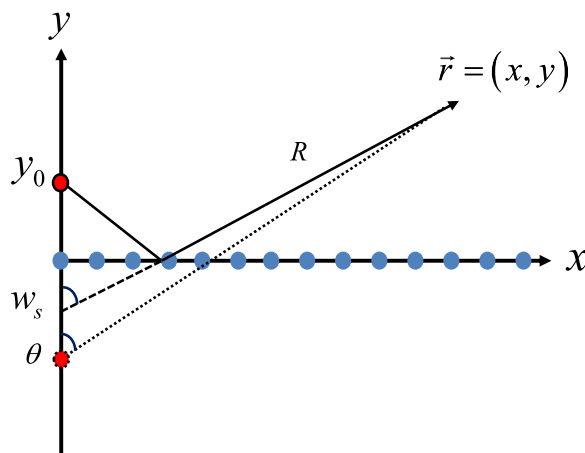


FIG. 6. The polar coordinate system.

A. Spectral representation and the source field

We assume that a line source is located above the wire surface at $y = y_0, x = 0$ (in the following numerical examples we set $y_0 = \lambda^0/3$). The current density of the line source can be expressed formally by $\vec{J}_s = \hat{z}I_s\delta(y - y_0)\delta(x)$, where δ denotes Dirac's delta function. We utilize the theory of electromagnetic wave propagation in plane stratified media to analyze this excitation problem. Since the problem exhibits shift invariance in the z coordinate, Maxwell's equations are simplified,

$$\hat{x}\frac{\partial E_z}{\partial y} - \hat{y}\frac{\partial E_z}{\partial x} = -j\omega\mu(\hat{x}H_x + \hat{y}H_y), \quad (50a)$$

$$\hat{z}\left(\frac{\partial H_y}{\partial x} - \frac{\partial H_x}{\partial y}\right) = j\omega\varepsilon\hat{z}E_z + \hat{z}J_z. \quad (50b)$$

We expand the field using the Fourier kernel,

$$\Phi(x, k_x) = \frac{1}{\sqrt{2\pi}}e^{-jk_x x}. \quad (51)$$

The spectral field via the transformation pair,

$$\tilde{E}_z(k_x, y) = \int_{-\infty}^{\infty} E(x, y)\Phi^*(x, k_x)dx, \quad (52a)$$

$$E_z(x, y) = \int_{-\infty}^{\infty} \tilde{E}(k_x, y)\Phi(x, k_x)dk_x. \quad (52b)$$

Maxwell's equations (50) then reduce to

$$\frac{\partial \tilde{E}_z}{\partial y} = -j\omega\mu\tilde{H}_x, \quad (53a)$$

$$k_x\tilde{E}_z = -\omega\mu\tilde{H}_y, \quad (53b)$$

$$-\frac{\partial \tilde{H}_x}{\partial y} - jk_x\tilde{H}_y = j\omega\varepsilon\tilde{E}_z + \tilde{J}_z. \quad (53c)$$

We can write a set of equations for the tangential components,

$$\frac{\partial \tilde{E}_z}{\partial y} = -j\omega\mu\tilde{H}_x, \quad (54a)$$

$$-\frac{\partial \tilde{H}_x}{\partial y} - j\omega\varepsilon\left(1 - \frac{k_x^2}{k^2}\right)\tilde{E}_z = \tilde{J}_z, \quad (54b)$$

which immediately leads to the second-order differential equation for the electric field,

$$\frac{\partial^2 \tilde{E}_z}{\partial y^2} + k_y^2\tilde{E}_z = \frac{j\omega\mu I_s}{\sqrt{2\pi}}\delta(y - y_0) \quad (55)$$

with $k_y^2 = k^2 - k_x^2$. The solution to the inhomogeneous equation (55) can be expressed as the solution to the corresponding homogenous (source free) equation in two separate domains, $y > y_0$ and $y < y_0$ that are subject to the following two boundary conditions at $y = y_0$, $\frac{\partial \tilde{E}_z}{\partial y}(y_0^+) - \frac{\partial \tilde{E}_z}{\partial y}(y_0^-) = \frac{j\omega\mu I_s}{\sqrt{2\pi}}$ and $\tilde{E}_z(y_0^+) - \tilde{E}_z(y_0^-) = 0$. This leads quickly to the exact solution of the inhomogeneous equation,

$$\tilde{E}_z = \frac{\omega\mu I_s e^{-jk_y|y-y_0|}}{2\sqrt{2\pi}k_y}. \quad (56)$$

This solution is basically the spectral plane wave decomposition of the electric field excited in free space by a 2D, current line, source.

B. The scattered field—Spectral representation

Equation (56) provides the spectral plane wave amplitudes required to construct the line source field. Using the linearity of the problem, we can cast the scattered field by the spatiotemporal modulated grid simply by applying the scattering theory developed in the previous sections for each of the impinging plane waves that construct the source field. Then, we will integrate over the spectral parameter in order to go back to the physical space domain.

By Eq. (56), the impinging wave amplitude on $y = 0$, for a plane wave with spectral parameter k_x , reads

$$\tilde{E}_z^i = -\frac{\omega\mu I_s}{2k_y\sqrt{2\pi}}e^{-jk_y y_0}. \quad (57)$$

Once the impinging plane wave is known, including its direction of arrival, that is encoded by the spectral parameter k_x , we can directly apply the result in Eq. (41) in order to obtain the scattered field amplitude, for the spectral parameter k_x , for any frequency harmonic n , and taking into account the synthetic motion effect by the spatiotemporal modulation of the grid. This reads

$$\tilde{E}_n^{\text{scat}}(\vec{r}) = \frac{I_s\eta^2 k_0 k_n \tilde{A}_n e^{-jk_0 y_0} e^{-j(k_n x + k_n y)}}{a\sqrt{32\pi}k_{n,y}k_{0,y}}. \quad (58)$$

The sum over the spectral components constructs the scattered field by the 2D point source,

$$E_n^{\text{scat}}(\vec{r}) = \frac{I_s\eta^2 k_0 k_n}{8\pi a} \int_{-\infty}^{\infty} \frac{\tilde{A}_n e^{-jk_0 y_0} e^{-j(k_n x + k_0 y)}}{k_{n,y}k_{0,y}} dk_x \quad (59)$$

and the sum over the index n , i.e., the time harmonics multiplied by their proper time dependency, yields the total field in space and time. Here,

$$k_{n,x} = k_x + n\frac{\Delta\varphi}{a}, \quad (60a)$$

$$k_{n,y} = \sqrt{k_n^2 - k_{n,x}^2}. \quad (60b)$$

Regarding the last steps in the derivation, we note that although the frequency response seems to have some analogy to nonlinear Raman medium due to the multiple time harmonics that are excited [56,57], here the system is linear time variant (LTV) and therefore the principle of superposition in time strictly applies. One possible way to consider that is by assuming a strong pump signal that modulates a nonlinear medium in time, and much weaker signals that are manipulated by this effective time-varying medium. With respect to these weak signals the systems is linear time variant.

We now compare three different calculations, to examine our analysis. In the following we focus on scenarios with $n_r = 1$ since it leads to more efficient power delivery. We evaluate the excited field by the local 2D wire source in three different ways:

(1) By a quasifrequency domain (QFD) full-wave simulation of a finite spatiotemporal wire grid with 401 wires. For

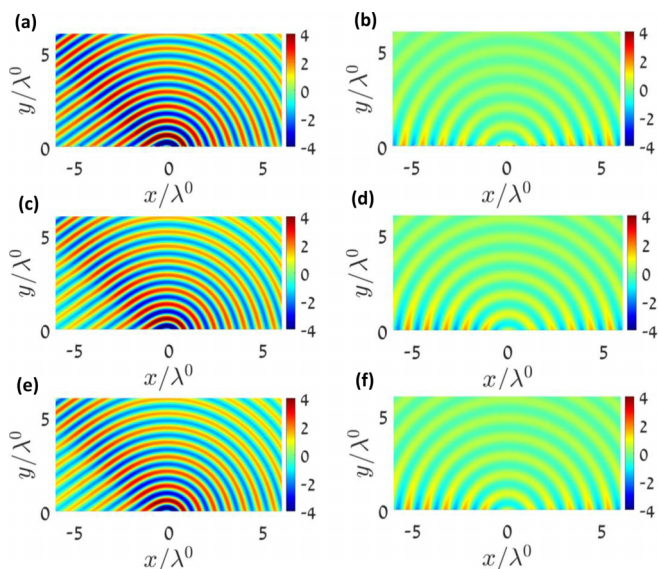


FIG. 7. Case I. The real part of the scattered electric field for the resonance harmonic, normalized with the absolute value of the scattered stationary field for $n = 0$ at the origin. (a) QFD simulation for the resonance harmonic. (b) QFD simulation for the fundamental frequency. (c) Integration over the exact currents for the resonance harmonic. (d) Integration over the exact currents for the fundamental frequency. (e) Integration over the approximated currents for the resonance harmonic. (f) Integration over the approximated currents for the fundamental frequency.

this simulation, an harmonic balance approach combined with a simple version of the method of moments was utilized. See details in [10].

(2) By a direct integration of Eq. (59), with the exact currents, which previously calculated via the inverse of the matrix $\underline{U}^{(N)}$ for a large N (we used $N = 3$). In order to avoid singularities in our integration near $k_x = k_0$, we deform our integration contour, with $k_x \rightarrow k_x + j\frac{2\varepsilon}{\pi} \arctan k_x$, where $\varepsilon \ll \frac{\pi}{2}k_0$ (in our case, we have chosen $\varepsilon = 0.001\frac{\pi}{2}k_0$).

(3) By a direct integration as in the previous paragraph, but with the approximated currents from Eqs. (34)–(35).

The results obtained by the aforementioned three calculation approaches are depicted in Fig. 7 for Case I, and in Fig. 8 for Case II, with the corresponding parameters given in Table I. In both cases, a good agreement between the calculations is seen. This establishes the accuracy of the spectral representation and in particular, the approximations for the induced current on the wires as discussed in detail in the preceding sections above. At this point, we are ready to analyze asymptotically the spectral integral. This is done in the following section.

C. The physical interpretation of the singular and critical points in the complex spectral plane

After confirming numerically the sufficient accuracy of the direct spectral integration over the approximate current in Eqs. (34)–(35), we can now turn to analyze the contribution of each critical point in the complex spectral plane to the different wave creatures that are excited and propagated in

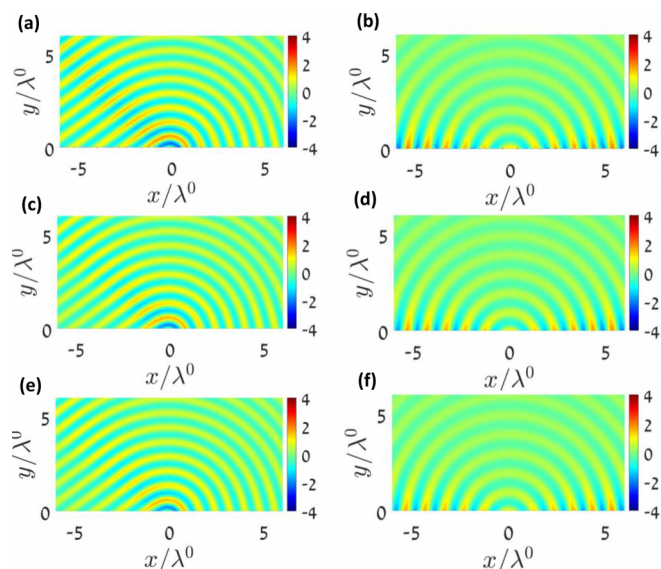


FIG. 8. Case II. The real part of the scattered electric field for the resonance harmonic, normalized with the absolute value of the scattered stationary field for $n = 0$ at the origin. (a) QFD simulation for the resonance harmonic. (b) QFD simulation for the fundamental frequency. (c) Integration over the exact currents for the resonance harmonic. (d) Integration over the exact currents for the fundamental frequency. (e) Integration over the approximated currents for the resonance harmonic. (f) Integration over the approximated currents for the fundamental frequency.

our system. These critical points are branch points, poles, and stationary points. Interestingly, we reveal peculiar differences between the two cases shown in Table I, of high and low transfer ratio.

First, note that $k_{n,y}$ in Eq. (60) involves two, generally asymmetric, branch points, $k_x = \pm k_n - n\Delta\phi/a$, for each frequency harmonic n . In particular, for $n = 0$, $k_{0,y}$ the branch points become symmetric and located at $k_x = \pm k_0$. The branch points for the $n = 0$ harmonic can be eliminated by introducing a transformation to the complex w angle plane [45]. Specifically, we define $k_x = k_0 \sin w$. Then, $k_{0,y} = k_y = k_0 \cos w$, and contains no branch point in the complex w plane. Under this transformation, the integration path termed the Sommerfeld integration path (SIP), takes the form shown in Fig. 9.

Let us now define the following polar coordinates transformation: $x = R \sin \theta$, $y = R \cos \theta - y_0$, where θ is the angle of specular reflection by a stationary uniform impedance surface (i.e., if the angle of incidence equals to the angle of reflection) as it can be seen in Fig. 6. We can now use Eq. (34) and write the integral in Eq. (59) by

$$E_1^{\text{scat}}(\vec{r}) = -\frac{I_s \eta k_0}{4\pi} \int_{\text{SIP}} \frac{e^{-j[k_{0,y}(w)y_0 + k_{1,x}(w)x + k_{1,y}(w)y]} dw}{\frac{b_0}{a_1} - \frac{c_0}{b_1} - \frac{a_2 c_1 b_0}{a_1 b_1 b_2}} \quad (61)$$

where a_1, a_2, b_0, b_1, b_2 , and c_0, c_1 are given in Eq. (21), and are all functions of w . This integral has the canonical form of

$$I = \int_{\text{SIP}} f(w) e^{-jq(w)} dw, \quad (62)$$

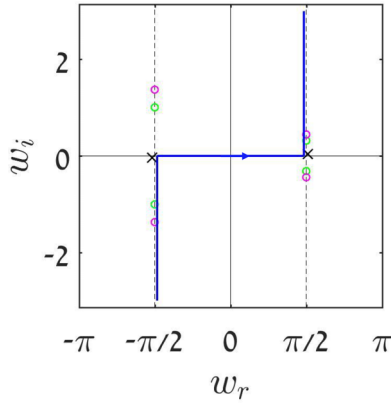


FIG. 9. The complex angle plane w . The Sommerfeld integration path (SIP) is shown by the blue line. The branch points, in green circles [of $k_{1,y}(w)$] and in pink circles [of $k_{2,y}(w)$], are shown to be asymmetrically located due to the synthetic motion. The branch cuts (not drawn) originate from the branch points and extending to infinity. Two poles are also shown by black crosses, located slightly off the real axis, correspond to strong excitations, leaky but not guided modes. These solutions contribute asymptotically only for grazing angle observer, and only under certain modulation conditions. Interestingly, as shown below, in the asymptotic evaluation of the spectral integral, due to the synthetic motion it occurs that a pole may contribute asymptotically for a certain observer but not contribute for another observer symmetrically located around the source.

where w is the complex integration variable, and $f(w)$ and $q(w)$ represent the amplitude and phase functions that are assumed to be slowly varying. In Eq. (61), q represents the phase term in the squared brackets. For remote observer, q asymptotically grows with the distance. In order to explore the analytic properties of the integral we first have to identify the singular points of the integrand, i.e., branch points and poles. We note that although we focus on $n_r = 1$, the integrand also depends on $b_2(w)$ [which is associated with the second, $n = 2$, harmonic—see Eq. (21)], and therefore, in light of the definition of $k_{n,y}$ in Eq. (60), we have two sets of branch points to consider. We also note that, unlike the stationary case, here the branch points affect also $q(w)$, since $k_{1,y}(w)$ has a branch point. This phenomenon, along with the resonance of b_1 , leads to a much stronger influence of the branch point in $k_{1,y}(w)$ than the one in $k_{2,y}(w)$. This can be explained by the fact that the high Q implies large imaginary part of $k_{2,y}$ since the resonance is in the $n = 1$ harmonic rather than the $n = 2$ one. Consequently, when the square root in $k_{2,y}$ nullifies, yet the value of b_2 remains practically unchanged. Note that the numerical calculation below takes both branch cut contributions into account, as opposed to the analytic asymptotic evaluation that is also provided below. We also note that the branch points do not depend on the quality factor, so they are the same for both cases shown in Table I. The branch points are: $w_b = \arcsin \frac{k_n - n \frac{\Delta\varphi}{a}}{k_0}$, $\pi - \arcsin \frac{k_n - n \frac{\Delta\varphi}{a}}{k_0}$, $-\arcsin \frac{k_n + n \frac{\Delta\varphi}{a}}{k_0}$, $-\pi + \arcsin \frac{k_n + n \frac{\Delta\varphi}{a}}{k_0}$. Using the parameters we assume above for the cases in Table I, the branch points due to $k_{1,y}(w)$ are $\frac{\pi}{2} \pm 0.31j$, $-\frac{\pi}{2} \pm j$, and due to $k_{2,y}(w)$ are $\frac{\pi}{2} \pm 0.44j$, $-\frac{\pi}{2} \pm 1.37j$ for $\frac{\pi}{2} \pm 0.44j$, $-\frac{\pi}{2} \pm 1.37j$. Next, we turn to find the

pole locations. This calculation is somewhat more complicated but can be simplified using the approximation that the poles are near the point w_{p0} that satisfies $b_0(w_{p0}) = 0$. Specifically, we find that $w_{p0} = \pm \arccos \frac{j\eta}{2a(\omega_0 \tilde{L} - \frac{1}{\omega_0 c})}$, since $\frac{c_0}{b_1(w)} \ll 1$ near w_{p0} (because of the high quality factor). Therefore, we can write $w_p = w_{p0} + \delta w_p$, substitute in the denominator of Eq. (61) and demand equality to zero. This leads to the following perturbational expression for the poles:

$$w_p \approx \pm \arccos \frac{j\eta}{2a(\omega_0 \tilde{L} - \frac{1}{\omega_0 c})} + \frac{a_1 c_0}{b_1(w_{p0}) \left[1 - \frac{a_2 c_1}{b_1(w_{p0}) b_2(w_{p0})} \right] \frac{\eta \sin w_{p0}}{2a \cos^2 w_{p0}}}. \tag{63}$$

For the parameters given in Table I, this approximate calculation gives $w_p = 1.59 + 0.13j$, $-1.62 - 0.14j$, whereas a brute force numerical search for the poles gives $w_p = 1.58 + 0.13j$, $-1.62 - 0.12j$. Figure 9 depicts the singular points, i.e., branch points, and poles, on the w plane.

Remark 1. As discussed below, we define the corresponding cuts of the plotted branch points lie strictly on the $w_r = \pm \pi/2$, and therefore we consider the SIP trajectory to be located slightly in the interior for the stripe defined by $-\pi/2 \leq w_r \leq \pi/2$.

We now aim to find the saddle point w_s of the integrand in Eq. (61). At the saddle point, the phase term derivative with respect to the spectral variable nullifies, i.e., we demand $q'(w) = 0$, where

$$q' = -k_0 y_0 \sin w + k_0 x w \sin \theta - \frac{k_{1,x}(w) k_0 y \cos w}{k_{1,y}(w)}, \tag{64}$$

where $k_{1,x}(w)$ and $k_{1,y}(w)$ are given in Eq. (60) with $k_x = k_0 \sin w$. Without loss of generality, we narrow ourselves to the case of positive phase accumulation $\Delta\varphi > 0$. We use the intermediate value theorem to show that for every observation point (x, y) there is a real valued saddle point in the visible range at the nominal frequency, i.e., $-k_0 < k_{0,x} < k_0$ ($-\frac{\pi}{2} < w < \frac{\pi}{2}$). Specifically, we note that obviously $q'(w = \frac{\pi}{2}) = -y_0$, $q'(w = -\frac{\pi}{2}) = y_0$. Next, since we narrowed ourselves to the case of slow synthetic motion, i.e., $\Delta\varphi < (k_n - k_0)a$, the square root in Eq. (64) (i.e., the $k_{1,y}$ term) is real and positive. Therefore, there must exist a w value in the visible range, which fulfils the saddle point condition of $q' = 0$. However, the physical picture alters for fast synthetic motion, which is outside the scope of the current paper. Returning to slow synthetic motion; for the case where the saddle point value is far from nullifying the square root in Eq. (64), we can approximate the saddle point location using the assumption of small deviation δw from the specular angle θ . To that end we first assume a small correction over the specular reflection, i.e., $w_s = \theta + \delta w_s$. Next we use the following Taylor approximations $\sin(\theta + \delta w) \approx \sin \theta + \delta w \cos \theta$, $\cos(\theta + \delta w) \approx \cos \theta - \delta w \sin \theta$. Clearly, for $n = 0$, $\delta w_s = 0$. We can express approximately the spectral wave vectors components, with a second-order Taylor expansion, in order to easily calculate the stationary point (see Appendix C).

Thus, we get the small deviation from the specular angle for the resonance harmonic,

$$\delta w_s = \frac{\left[y_0 \sin \theta - R \sin \theta \cos \theta + \frac{k_{1,x}(\theta) \cos \theta}{k_{1,y}(\theta)} (R \cos \theta - y_0) \right]}{\left\{ -y_0 \cos \theta - R \sin^2 \theta - \left[\frac{k_0 \cos^2 \theta - k_{1,x}(\theta) \sin \theta}{k_{1,y}(\theta)} + \frac{(k_{1,x}(\theta))^2 k_0 \cos^2 \theta}{(k_{1,y}(\theta))^3} \right] (R \cos \theta - y_0) \right\}}. \tag{65}$$

In the following numerical calculations for the Green's function, despite having this approximation for the saddle point location, we in fact solve numerically the equation $q'(w) = 0$. Nevertheless, the approximation in Eq. (65) is of importance since it highlights quantitatively important physical observations. First, in asymptotic terms, the saddle point provides the angle of the ray that leaves the source, impinges the reflecting layer, and approaches the observer. The introduction of an effective synthetic motion yields asymmetric scattering, which is evident by the asymmetry of δw_s with respect to θ in Eq. (65). Second, by observation in Eq. (65), as well as in Fig. 10, it is seen that the asymmetric scattering effect caused by the saddle point contribution ("reflected ray") is negligible right on the boundary since the saddle point location is nearly symmetric there. This effect becomes dominant at moderated distances $\sim 1 - 2\lambda_0$ (see the bluish asymmetric finite angular sectors in Fig. 10).

Once the saddle point is known, we seek next to find the steepest descent path (SDP), along which the integrand is not oscillatory, instead, it is monotonically increasing up to a maximal value at the saddle point and then monotonically decreasing to zero, passing between two valleys in the complex w plane. This will be useful in the numerical calculation of the deflected ray field that travels from the sources, hits the spatiotemporally modulated surface, and reflected to the observer. In order to find the SDP, we follow the standard recipe that is described for example in [45]. On the SDP, by definition, $q(w) = q(w_s) - js^2$, with $s \in (-\infty, \infty)$ denoting a real variable along the path. As s goes from $-\infty$ to $+\infty$, the integrand in Eq. (59) exhibits a Gaussian like behavior, with a fast decaying integrand away from the stationary point.

The synthetic motion by the spatiotemporal modulation creates asymmetry in the complex w plane not only in the saddle point location (as discussed above) but also in the branch points and pole locations. To demonstrate that we shall now explore six different observation point locations in space; three of which [(a)–(c)] with a positive angle θ , and additional

three [(d)–(f)] that are mirror-symmetrically located about the y axis with negative θ (see Fig. 6). These observation locations in cartesian coordinates normalized with respect to the wavelength λ_0 , i.e., $(x, y)/\lambda_0$, are: (a),(d) $(\pm 3, 2)$, (b),(e) $(\pm 3, 0.3)$, and lastly, (c),(f) $(\pm 6, 0.15)$. For each observation point we calculate the total spectral integral, as well as the three isolated integration components by which it is composed, i.e., an integration along the SDP, integration around the branch cuts, and lastly pole residues if required. The analysis is done for the two cases of energy transfer ratio T_1 [see Eq. (36)] between the fundamental and first harmonics, with parameters given in Table I.

In Figs. 11 and 12 we bring the map of the integration path as well as the singular points. We clearly see the asymmetry in the complex plane and the SDP path between observers that

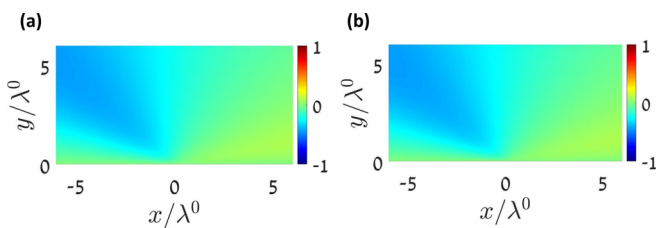


FIG. 10. δw_s for a continuum of observation points (x, y) . (a) Calculation by Eq. (65) with parameters given in Table I Case I. (b) As in (a) but for Case II. The difference between the cases is visually negligible. However, in both cases the asymmetric scattering contribution by the saddle point is evident.

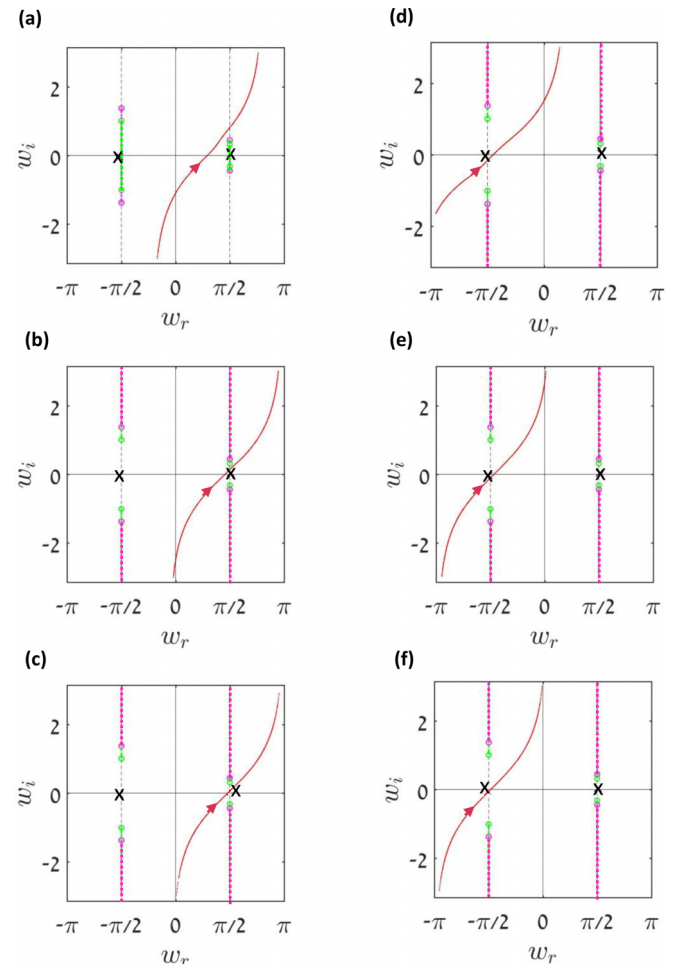


FIG. 11. Case 1 (high transfer ratio). The complex plane, including the SDP path, branch points, in the complex plane for six observation points listed by [(a)–(f)] in the text.

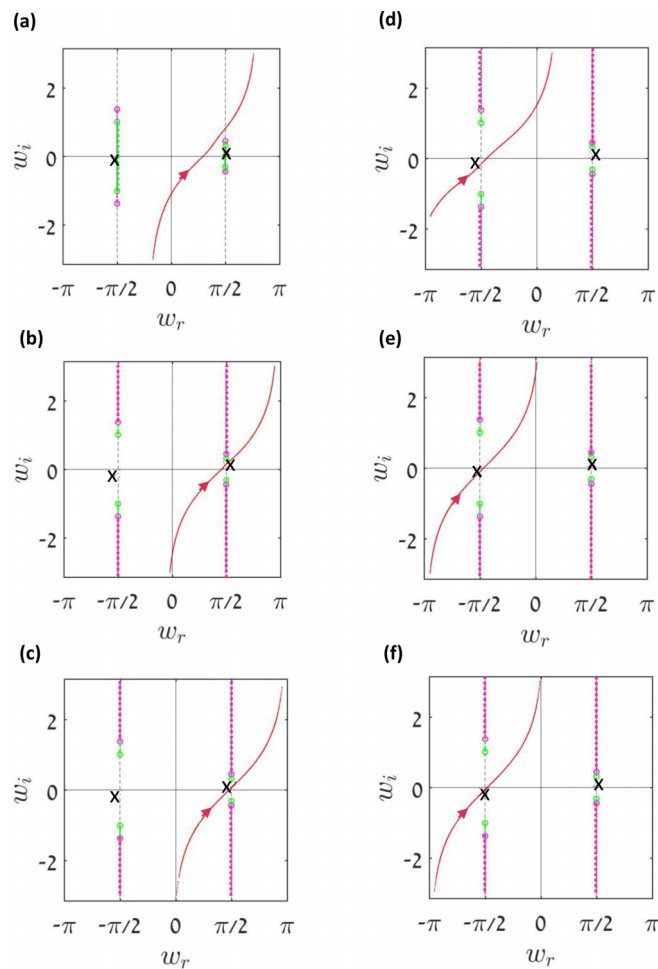


FIG. 12. As in Fig. 11 but with parameters corresponding to Case 2 (low transfer ratio).

are located symmetrically about the y axis (with positive and negative θ).

As opposed to the spectral representation in LTI layered media that is on-plane homogenous (normal to the layers axis), here, the phase term also contains branch point singularities. Nevertheless, the SDP should obviously remain continuous. Otherwise, Cauchy principle that is used in order to connect the SDP integration, the branch cut integrations, and poles integrations with the original SIP integral, will not be applicable. To address this issue, we uniquely define the branch cut of $k_{1,y}$ such that the square root results a positive or negative real part in the upper Riemann sheet, in a manner that the SDP will not cross the branch cut trajectories. This is demonstrated in Figs. 11 and 12 where the SDP trajectories are shown with the singular points on the complex w plane. Note that the map shown in Fig. 11(a) is exceptional compare to the maps shown in Figs. 11(b)–11(f) in the branch cut form that originates from different upper Riemann sheet definition. For (a) we chose $\text{Re}\{k_{1,y}\} < 0$ on the upper sheet, while for Figs. 11(b)–11(f) we chose the opposite definition. By this choice, the SDP trajectory does not cross branch cut singularities and thus remains continuous. The same is true for Fig. 12. This choice also determines whether or not the branch cut contribution should be included in the spectral

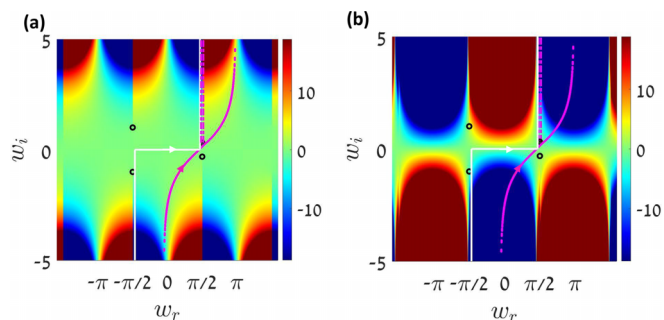


FIG. 13. Integration path of the branch cut numerical integration—low positive θ . (a) $k_{1,y}(w)$. (b) $q(w)$. Here we can calculate the integral directly, following the path around the branch cut.

integral (for detailed discussion in this context, see e.g., [45]). To explain that, recall *Remark 1* above about the location of the SIP path and the branch cuts, and note the complex plane map in Fig. 11(a). At infinity, the SDP and SIP can be directly connected without crossing of a branch cut. Therefore, the SIP integral is simply given by the SDP integral (no pole is encircled in this case). In contrast, in Figs. 11(b)–(f) the SDP can be connected to the SIP without branch cut crossing only by encircling of the upper branch cuts on $w_r = +\pi/2$ [Figs. 11(b) and 11(c)], or the lower branch cuts on $w_r = -\pi/2$ [Figs. 11(d)–(f)]. Another important numerical point should be discussed in the context of the branch cut contributions. Note that our upper sheet definition by dictating the sign of the real part of the square root implies that both in the upper, and lower, Riemann sheets the integrand may diverge. However, when we connect the SIP path with the SDP path the branch cut encircling integration, at infinity, we have to make sure that the connecting paths are within a valley of the integrand in the complex w plane, and thus their contributions are vanishingly small. This situations that corresponds, for example, to the parameters in Case I and observation point b in Table I is illustrated in Fig. 13. In (a) the real part of $k_{1,y}(w)$ is shown to highlight the branch cut discontinuities, and in (b) the imaginary part of the phase function $\text{Im}\{q(w)\}$ is shown. Note that $\text{Im}\{q(w)\} < 0$ implies exponential decay of the integrand as $w \rightarrow \infty$, while $\text{Im}\{q(w)\} > 0$ implies exponential divergence. In the case shown in Fig. 13(b), the two sides of the upper branch cut at $w_r = \pi/2$ are located in a valley, and the connection of the integration paths is trivial. The situation is more challenging for example with the parameters of Case I observation point (d). This is illustrated in Fig. 14. In (a) the real part of $k_{1,y}(w)$ is shown to highlight the branch cut discontinuities, and in (b) the phase function $q(w)$ is shown. In this case, between the lower branch cut at $w_r = -\pi/2$ and the SDP trajectory at infinity, there is a divergence of the integrand. The numerical resort in this case is to integrate around the branch cut along a thicker path, as shown in Fig. 14(b); a path that goes around the branch cut from one valley to another valley.

In Table II we bring a numerical comparison between the direct numerical solution of the integral in Eq. (59), where the current is calculated by Eq. (34), and the sum of the isolated components: SDP integral, branch cut integral, and pole residues.

TABLE II. Comparison of the exact integral calculation to the sum of the SDP, branch cut and pole contributions.

	Direct	SDP	Branch cut	Pole	Relative Err
Case I(a)	-95 +8j	-95 +8j			0
Case I(b)	-98+55j	-97+67j	1-11j		0.002
Case I(c)	-85+4j	-81	-4-4j		0.006
Case I(d)	-94-59j	-88-62j	-6+2j		0.009
Case I(e)	-51+68j	-51+68j	0		0
Case I(f)	-40+46j	-40+46j	0		0
Case II(a)	-96 +11j	-96 +11j			0
Case II(b)	-91+88j	-93+98j	-13j		0.02
Case II(c)	-99+41	-16-25j	-4-5j	-80+73j	0.02
Case II(d)	-116-54j	-109-56j	-7+2j		0
Case II(e)	-40+92j	-42+91j	1		0.02
Case II(f)	-73+22j	2-34j	0	-75+54j	0.02

We can see a very good agreement between the two calculations, as it is evident by error obtained when summing up the three contributions SDP, branch cut, and poles to the direct spectral integration. The asymmetry of the singular points and the SDP for mirror observer locations is so evident by noting that in certain conditions the branch cut or pole contributions exist for observer location at a certain point, but do not exist at all, for observer that is located in the symmetric location point. This happens for instance in Case I(a) vs Case I(d) for the branch cut contribution. Regarding the poles, for the selected parameters, they pop up on the upper Riemann sheet under very specific conditions, with high angle θ (nearly grazing incidence—i.e., source and observer are located very close to the surface compare to the distance between them), and with low energy transfer rate. For the pole contribution, we can get an analytical expression, using the Cauchy residue theorem [45],

$$E_{1,p}^{scat} = -\frac{jI_s \eta k_0 H}{2} \frac{e^{-j[k_{0,y}y_0 + k_{1,x}x + k_{1,y}y]}}{\frac{b'_0}{a_1} + \frac{c_0 b'_1}{b_1^2} - \frac{a_2 c_1}{a_1} \left[\frac{b'_0 b_1 b_2 - b_0 (b'_1 b_2 + b_1 b'_2)}{b_1^2 b_2^2} \right]}, \tag{66}$$

As we can see in Table II in Case II(c) and Case II(f), when grazing the surface, the pole has a critical effect. When

comparing to Cases I(c) and I(f), we see that there is no contribution by pole singularity in these cases. This is interesting since Cases I and II are identical, except for the transfer ratio between the first and fundamental harmonics, T_1 , which is 12 dB in Case I and 6 dB in Case II.

It is then of interest to estimate, per a given source and observer heights, y_0 and y , respectively, the distance x_p after which the pole is captured between the SDP and the SIP. As a first approximation, we estimate the derivative of q in Eq. (64) by substituting $y = 0$ (which makes sense since we are dealing with grazing angles),

$$q' = -k_0 y_0 \sin w + k_0 x \cos w = 0. \tag{67}$$

This leads to a close form zeroth-order approximation for the stationary point $w_s = \arctan \frac{x}{y_0}$. By plugging in the expression for $q(w)$ we get

$$q_s = \begin{cases} \frac{k_0 y_0^2}{x} + [k_0 + n \frac{\Delta \varphi}{a}] x & \theta > 0 \\ -\frac{k_0 y_0^2}{x} + [-k_0 + n \frac{\Delta \varphi}{a}] x & \theta < 0 \end{cases}. \tag{68}$$

We can now demand $\text{Re}\{q(w_p)\} = q_s$, where w_p is given in Eq. (63). We get an estimation for the distance in which the pole becomes effective,

$$x_{\text{pol}} = \begin{cases} y_0 \frac{-\cos w_{p,r} \cosh w_{p,i} \pm \sqrt{(\cos w_{p,r} \cosh w_{p,i})^2 + 4(\sin w_{p,r} \cosh w_{p,i} - 1)}}{2(\sin w_{p,r} \cosh w_{p,i} - 1)} & \theta > 0 \\ y_0 \frac{-\cos w_{p,r} \cosh w_{p,i} \pm \sqrt{(\cos w_{p,r} \cosh w_{p,i})^2 - 4(\sin w_{p,r} \cosh w_{p,i} + 1)}}{2(\sin w_{p,r} \cosh w_{p,i} + 1)} & \theta < 0 \end{cases}. \tag{69}$$

For the case of high transfer ratio, we get $x_{\text{pol}} = 13.6\lambda_0$ for $\theta > 0$. An interesting phenomenon is that for $\theta < 0$ there is no distance in which a pole contribution emerge—the result for x_{pol} is complex. For the case of low transfer ratio we get $x_{\text{pol}} = 3.9\lambda_0$ for $\theta > 0$ and $x_{\text{pol}} = -5.9\lambda_0$ for $\theta < 0$. This provides a quick explanation why in Table II there is no pole contribution in some of the cases.

D. Asymptotic evaluation

In this section we present method for asymptotic evaluation of the expressions from the previous section, and their limitations. We focus on the SDP integral and the branch cut contribution [we have already evaluated analytically the pole contribution in Eq. (66)]. We evaluate asymptotically the integral along the SDP. For the integral in Eq. (62) with

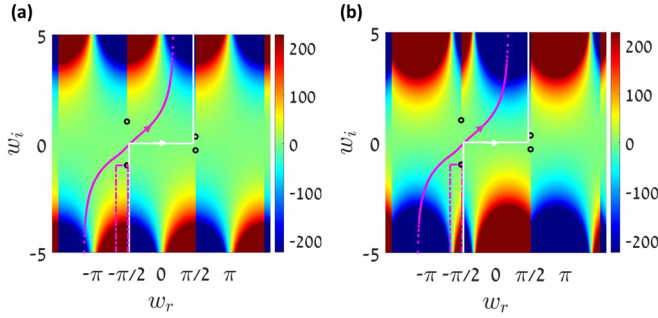


FIG. 14. Integration path of the branch cut numerical integration—high negative θ . (a) $k_{1,y}(w)$. (b) $q(w)$. Here the integration can not follow closely to the branch cut, since q has high positive imaginary part, which leads to diverging of the integration.

$|q\psi| \gg 1$, the SDP contribution can be approximated by [45]

$$I_{\text{SDP}} \approx e^{-j\frac{\pi}{4}} \sqrt{\frac{2\pi}{\psi q''(w_s)}} f(w_s) e^{-j\psi q(w_s)}. \quad (70)$$

Where w_s is the saddle point. We note that this approximation assumes that f is slowly varying near the saddle point, which is true only far from the singularities in the complex plane. Therefore, this approximation is only valid for large enough θ . We use the algebra from Appendix C to calculate the second derivative of q . In this approximation, since we used second-order Taylor expansion, the second derivative does not depend on δw_s ,

$$q''(\theta) = -y_0 k_0 \cos \theta - k_0 R \sin^2 \theta - \left[\frac{k_0^2 \cos^2 \theta - k_{n,x}(\theta) k_0 \sin \theta}{k_{n,y}(\theta)} + \frac{(k_{n,x}(\theta))^2 k_0^2 \cos^2 \theta}{(k_{n,y}(\theta))^3} \right] (R \cos \theta - y_0). \quad (71)$$

$$E_{1,\text{branch}}^{\text{scat}} = \begin{cases} \frac{I_s \eta a_1 y (k_0 \sin w_b + \frac{\Delta \varphi}{a}) \sqrt{\cos w_b} e^{-j[k_0 y_0 \cos w + (k_0 \sin w + \frac{\Delta \varphi}{a})x]} e^{j\frac{3}{2} \arg\{-j(-y_0 \sin w_b + x \cos w_b)\}}}{2\sqrt{\pi} b_0 | -y_0 \sin w_b + x \cos w_b |^{\frac{3}{2}} \sqrt{k_1 + (k_0 \sin w_b + \frac{\Delta \varphi}{a})}} & \theta > 0 \\ \frac{j I_s \eta a_1 y (k_0 \sin w_b + \frac{\Delta \varphi}{a}) \sqrt{\cos w_b} e^{-j[k_0 y_0 \cos w + (k_0 \sin w + \frac{\Delta \varphi}{a})x]} e^{j\frac{3}{2} \arg\{-j(-y_0 \sin w_b + x \cos w_b)\}}}{2\sqrt{\pi} b_0 | -y_0 \sin w_b + x \cos w_b |^{\frac{3}{2}} \sqrt{k_1 - (k_0 \sin w_b + \frac{\Delta \varphi}{a})}} & \theta < 0 \end{cases}. \quad (76)$$

When comparing the results from Table II for Case I(b) to the asymptotic expression in Eq. (76), we get a large relative error of about 10%. We note that for the case described at Fig. 14 [Case I(d)] we can not use this approximation.

VI. CONCLUSIONS AND OUTLOOK

In this paper we have developed a rigorous excitation theory for spatiotemporally modulated metasurface. The theory enables the derivation of the separated wave components that comprise the Green's function. From the mathematical standpoint these are related to different singularities and unique points in the complex spectral plane. Although here for the sake of concreteness we considered the Green's function due to a source above a metasurface, the theory can be applied

We can now write the approximate expression

$$E_{1,\text{SDP}}^{\text{scat}}(\vec{r}) = \frac{I_s \eta^2 k_0^2 k_1 \cos w_s}{8\pi a k_{1,y}(w_s) k_{0,y}(w_s)} \times \sqrt{\frac{2\pi}{q''(w_s)}} \tilde{A}_n(w_s) e^{-j\frac{\pi}{4}} \times e^{-j[k_{0,y}(w_s)y_0 + k_{n,x}(w_s)R \sin \theta + k_{n,y}(w_s)(R \cos \theta - y_0)]} \quad (72)$$

where $w_s = \theta + \delta w_s$. When comparing the results from Table II for Case I(a), which represent high positive θ we get a relative error of 0.03. We can now move to the approximation for the branch cut contribution. We focus on the branch cut of $k_{1,y}$, since as mentioned before, the contribution due to the branch cut of $k_{2,y}$ is negligible. We note that for the Canonical case where q is *regular*, the expression for the branch cut contribution is given by [45]

$$I_b = \frac{2\sqrt{\pi}}{|\psi q'(w_b)|^{\frac{3}{2}}} \sqrt{w - w_b} f'(w_b) e^{-j\psi q(w_b)} e^{j\frac{3}{2} \arg\{-jq'(w_b)\}}. \quad (73)$$

In our case, unfortunately, q involves branch cut singularities. Nevertheless, we can use the fact that asymptotically most of the contribution from the branch cut integration is caused by the integration in the close vicinity of the branch point. Therefore, we can approximate the integral with

$$E_{1,\text{branch}}^{\text{scat}}(\vec{r}) \approx -\frac{I_s \eta k_0 a_1 (1 - j k_{1,y}(w)y) e^{-j[k_{0,y}(w)y_0 + k_{n,x}(w)x]}}{4\pi \frac{b_0(w)}{b_1(w)} \left(b_1(w) - \frac{a_1 c_0}{b_0(w)} - \frac{a_2 c_1}{b_2(w)} \right)}. \quad (74)$$

Therefore, we define a new f with

$$f(w) = -\frac{I_s \eta k_0 a_1}{4\pi} \frac{(1 - j k_{1,y}(w)y)}{\frac{b_0}{b_1} \left(b_1 - \frac{a_1 c_0}{b_0} - \frac{a_2 c_1}{b_2} \right)}. \quad (75)$$

We can now apply the ordinary method to get the approximate branch cut contribution (see Appendix D)

to various excitation scenarios. Such as the excitation of a layered time and space-time modulated medium, etc. The advantage in having the Green's function is twofold. From the physical perspective it provides deeper understanding of the wave problem, while from the numerical perspective it may be useful in numerical schemes based on integral equations for the excitation and propagation in space-time modulated media. This is an important topic for a continuing research.

ACKNOWLEDGMENT

This research was supported by the Israel Science Foundation (Grant No. 1457/23).

We can now calculate $q'(\theta + \delta w_s)$ of the integral expression in Eq. (59),

$$q'(\theta + \delta w) = [-k_0 \sin \theta - k_0 \cos \theta \delta w]y_0 + (k_0 \cos \theta - k_0 \sin \theta \delta w)R \sin \theta + \left\{ \begin{aligned} & -\frac{k_{1,x}(\theta)k_0 \cos \theta}{k_{1,y}(\theta)} + \\ & \left[\frac{-k_0^2 \cos^2 \theta - k_{1,x}(\theta)k_0 \sin \theta}{k_{1,y}(\theta)} - \right. \\ & \left. \frac{(k_{1,x}(\theta))^2 k_0^2 \cos^2 \theta}{(k_{1,y}(\theta))^3} \right] (\delta w) \end{aligned} \right\} (R \cos \theta - y_0). \tag{C4}$$

The demand for $q' = 0$ leads to Eq. (65).

APPENDIX D: APPROXIMATE BRANCH CUT CALCULATION

We start with the derivative of $k_{1,y}$,

$$k_{1,y}' = -\frac{(k_0 \sin w + \frac{\Delta\varphi}{a})k_0 \cos w}{\sqrt{k_1^2 - (k_0 \sin w + \frac{\Delta\varphi}{a})^2}}. \tag{D1}$$

Using l'hopital's rule, we can write

$$k_{1,y}^{+'} \sim -\frac{(k_0 \sin w_b + \frac{\Delta\varphi}{a})k_0 \cos w_b}{\sqrt{k_1 + (k_0 \sin w_b + \frac{\Delta\varphi}{a})}\sqrt{-k_0 \cos w_b}} \frac{1}{\sqrt{w - w_b}}. \tag{D2a}$$

$$k_{1,y}^{-'} \sim -\frac{(k_0 \sin w_b + \frac{\Delta\varphi}{a})k_0 \cos w_b}{\sqrt{k_1 - (k_0 \sin w_b + \frac{\Delta\varphi}{a})}\sqrt{k_0 \cos w_b}} \frac{1}{\sqrt{w - w_b}}, \tag{D2b}$$

where $k_{1,y}^+$ represents the branch point for positive θ , and $k_{1,y}^-$ the negative θ . We can calculate the derivative of f from Eq. (76). After a little algebra,

$$f'(w_b) = -\frac{jI_s \eta k_0 a_1 y k_{1,y}'}{4\pi b_0}. \tag{D3}$$

Therefore

$$\sqrt{w - w_b} f'(w_b) = \begin{cases} \frac{I_s \eta k_0^{\frac{3}{2}} a_1 y}{4\pi b_0} \frac{(k_0 \sin w_b + \frac{\Delta\varphi}{a})\sqrt{\cos w_b}}{\sqrt{k_1 + (k_0 \sin w_b + \frac{\Delta\varphi}{a})}} & \theta > 0 \\ j \frac{I_s \eta k_0^{\frac{3}{2}} a_1 y}{4\pi b_0} \frac{(k_0 \sin w_b + \frac{\Delta\varphi}{a})\sqrt{\cos w_b}}{\sqrt{k_1 - (k_0 \sin w_b + \frac{\Delta\varphi}{a})}} & \theta < 0 \end{cases}. \tag{D4}$$

This leads to Eq. (76).

[1] Y. Ayasli, Field effect transistor circulators, *IEEE Trans. Magn.* **25**, 3242 (1989).
 [2] K. Gallo and G. Assanto, All-optical diode in a periodically poled lithium niobate waveguide, *Appl. Phys. Lett.* **79**, 314 (2001).
 [3] T. Kodera, D. L. Sounas, and C. Caloz, Artificial Faraday rotation using a ring metamaterial structure without static magnetic eld, *Appl. Phys. Lett.* **99**, 031114 (2011).
 [4] D. L. Sounas, T. Kodera, and C. Caloz, Electromagnetic modeling of a magnetless nonreciprocal gyrotropic metasurface, *IEEE Trans. Antennas Propag.* **61**, 221 (2013).
 [5] Z. Wang, Z. Wang, J. Wang, B. Zhang, J. Huangfu, J. D. Joannopoulos, M. Soljacic, and L. Ran, Gyrotropic response in the absence of a bias field, *Proc. Natl. Acad. Sci. USA* **109**, 13194 (2012).
 [6] B.-I. Popa and S. A. Cummer, Nonreciprocal active metamaterials, *Phys. Rev. B* **85**, 205101 (2012).
 [7] S. Manipatruni, J. T. Robinson, and M. Lipson, Optical nonreciprocity in optomechanical structures, *Phys. Rev. Lett.* **102**, 213903 (2009).
 [8] Y. Mazor and A. Alú, Nonreciprocal hyperbolic propagation over moving metasurfaces, *Phys. Rev. B* **99**, 045407 (2019).
 [9] R. Fleury, D. L. Sounas, C. F. Sieck, M. R. Haberman, and A. Alú, Sound isolation and giant linear nonreciprocity in a compact acoustic circulator, *Science*. **343**, 516 (2014).
 [10] M. Kreciczler and Y. Hadad, Wave analysis and homogenization of a spatiotemporally modulated wire medium, *Phys. Rev. Appl.* **16**, 054003 (2021).
 [11] S. Qin, Q. Xu, and Y. E. Wang, Nonreciprocal components with distributedly modulated capacitors, *IEEE Trans. Microw. Theory Techn.* **62**, 2260 (2014).
 [12] N. Reiskarimian and H. Krishnaswamy, Magnetic-free nonreciprocity based on staggered commutation, *Nat. Commun.* **7**, 11217 (2016).
 [13] Z. Yu and S. Fan, Complete optical isolation created by indirect interband photonic transitions, *Nat. Photon.* **3**, 91 (2009).
 [14] H. Lira, Z. Yu, S. Fan, and M. Lipson, Electrically driven nonreciprocity induced by interband photonic transition on a silicon chip, *Phys. Rev. Lett.* **109**, 033901 (2012).
 [15] D. L. Sounas, C. Caloz, and A. Alú, Giant non-reciprocity at the subwavelength scale using angular momentum-biased metamaterials, *Nat. Commun.* **4**, 2407 (2013).
 [16] N. A. Estep, D. L. Sounas, J. Soric, and A. Alú, Magnetic-free non-reciprocity and isolation based on parametrically modulated coupled-resonator loops, *Nat. Phys.* **10**, 923 (2014).
 [17] R. Sabri, M. M. Salary, and H. Mosallaei, Broadband continuous beam-steering with time-modulated metasurfaces in the near-infrared spectral regime, *APL Photonics* **6**, 086109 (2021).

- [18] H. Li, S. Yin, and A. Alú, Nonreciprocity and Faraday rotation at time interfaces, *Phys. Rev. Lett.* **128**, 173901 (2022).
- [19] H. He, S. Zhang, J. Qi, F. Bo, and H. Li, Faraday rotation in nonreciprocal photonic time-crystals, *Appl. Phys. Lett.* **122**, 051703 (2023).
- [20] F. R. Prudêncio and M. G. Silveirinha, Synthetic axion response with space-time crystals, *Phys. Rev. Appl.* **19**, 024031 (2023).
- [21] F. R. Prudêncio and M. G. Silveirinha, Replicating physical motion with Minkowskian isorefractive spacetime crystals, *Nanophotonics* **12**, 3007 (2023).
- [22] Y. Mazor and A. Alú, One-way hyperbolic metasurfaces based on synthetic motion, *IEEE Trans. Antennas Propagat.* **68**, 1739 (2020).
- [23] Y. Hadad, J. C. Soric, and A. Alu, Breaking temporal symmetries for emission and absorption, *Proc. Natl. Acad. Sci. USA* **113**, 3471 (2016).
- [24] Y. Hadad, D. L. Sounas, and A. Alu, Space-time gradient metasurfaces, *Phys. Rev. B* **92**, 100304(R) (2015).
- [25] S. Taravati, N. Chamanara, and C. Caloz, Nonreciprocal electromagnetic scattering from a periodically space-time modulated slab and application to a quasisonic isolator, *Phys. Rev. B* **96**, 165144 (2017).
- [26] S. Taravati and C. Caloz, Mixer-duplexer-antenna leaky-wave system based on periodic space-time modulation, *IEEE Trans. Antennas Propagat.* **65**, 442 (2017).
- [27] C. Caloz and Z. L. Deck-Leger, Spacetime metamaterials. Part I: General concepts, *IEEE Trans. Antennas Propagat.* **68**, 1569 (2019).
- [28] C. Caloz and Z. L. Deck-Leger, Spacetime metamaterials. Part II: Theory and applications, *IEEE Trans. Antennas Propagat.* **68**, 1583 (2019).
- [29] F. Monticone, N. M. Estakhri, and A. Alu, Full control of nanoscale optical transmission with a composite metascreen, *Phys. Rev. Lett.* **110**, 203903 (2013).
- [30] Y. Li, X. Jiang, R. Li, B. Liang, X. Zou, L. Yin, and J. Cheng, Experimental realization of full control of reflected wave with subwavelength acoustic metasurfaces, *Phys. Rev. Appl.* **2**, 064002 (2014).
- [31] C. Pfeiffer and A. Grbic, Millimeter-wave transmitarrays for wavefront and polarization control, *IEEE Trans. Antennas Propagat.* **61**, 4407 (2013).
- [32] M. Selvanayagam and G. V. Eleftheriades, Circuit modelling of Huygens surfaces, *IEEE Antennas Wireless Propag. Lett.* **12**, 1642 (2013).
- [33] M. Selvanayagam and G. V. Eleftheriades, Discontinuous electromagnetic fields using orthogonal electric and magnetic currents for wavefront manipulation, *Opt. Express* **21**, 14409 (2013).
- [34] C. Pfeiffer and A. Grbic, Metamaterial Huygens surfaces: Tailoring wave fronts with reactionless sheets, *Phys. Rev. Lett.* **110**, 197401 (2013).
- [35] D. Sievenpiper, J. Schaffner, R. Loo, G. Tansonan, S. Ontiveros, and R. Harold, A tunable impedance surface performing as a reconfigurable beam steering reflector, *IEEE Trans. Antennas Propagat.* **50**, 384 (2002).
- [36] E. Hasman, V. Kleoner, G. Biener, and A. Niv, Polarization dependent focusing lens by use of quantized Pancharatnam Berry phase diffractive optics, *Appl. Phys. Lett.* **82**, 328 (2003).
- [37] D. Lin, P. Fan, E. Hasman, and M. L. Brongersma, Dielectric gradient metasurface optical elements, *Science* **345**, 298 (2014).
- [38] J. P. S. Wong, M. Selvanayagam, and G. V. Eleftheriades, Design of unit cells and demonstration of methods for synthesizing Huygens metasurfaces, *Photonics Nanostruct. Fundam. Appl.* **12**, 360 (2014).
- [39] M. Kim, A. M. H. Wong, and G. V. Eleftheriades, Optical Huygens metasurfaces with independent control of the magnitude and phase of the local reflection coefficients, *Phys. Rev. X* **4**, 041042 (2014).
- [40] A. Epstein and G. V. Eleftheriades, Huygens metasurfaces via the equivalence principle: Design and applications, *J. Opt. Soc. Am. B* **33**, A31 (2016).
- [41] A. Epstein and G. V. Eleftheriades, Passive lossless Huygens metasurfaces for conversion of arbitrary source field to directive radiation, *IEEE Trans. Antennas Propagat.* **62**, 5680 (2014).
- [42] A. Epstein, J. P. S. Wong, and G. V. Eleftheriades, Cavity-excited Huygens metasurface antennas for near-unity aperture illumination efficiency from arbitrarily large apertures, *Nat. Commun.* **7**, 10360 (2016).
- [43] A. H. Dorrah, M. Chen, and G. V. Eleftheriades, Bianisotropic Huygens metasurface for wideband impedance matching between two dielectric media, *IEEE Trans. Antennas Propagat.* **66**, 4729 (2018).
- [44] D. L. Sounas, N. M. Estakhri, and A. Alú, Metasurfaces with engineered reflection and transmission: Optimal designs through coupled-mode analysis, in *2016 10th International Congress on Advanced Electromagnetic Materials in Microwaves and Optics (METAMATERIALS)*, Chania, Greece (IEEE, 2016), pp. 346–348.
- [45] L. B. Felsen and N. Marcuvits, *Radiation and Scattering of Waves* (IEEE Press series on electromagnetic waves, Piscataway, NJ, 1996).
- [46] B. T. Draine and P. J. Flatau, Discrete-dipole approximation for scattering calculations, *J. Opt. Soc. Am. A* **11**, 1491 (1994).
- [47] Y. Hadad and B. Z. Steinberg, Quasistatic resonance of a chemical potential interruption in a graphene layer and its polarizability: The mixed-polarity semilocalized plasmon, *Phys. Rev. B* **88**, 075439 (2013).
- [48] Y. Hadad and B. Z. Steinberg, Magnetized spiral chains of plasmonic ellipsoids for one-way optical waveguides, *Phys. Rev. Lett.* **105**, 233904 (2010).
- [49] Y. Mazor and B. Z. Steinberg, Longitudinal chirality, enhanced nonreciprocity, and nanoscale planar one-way plasmonic guiding, *Phys. Rev. B* **86**, 045120 (2012).
- [50] Y. Mazor, Y. Hadad, and B. Z. Steinberg, Planar one-way guiding in periodic particle arrays with asymmetric unit cell and general group-symmetry considerations, *Phys. Rev. B* **92**, 125129 (2015).
- [51] S. Tretyakov, *Analytical Modelling in Applied Electromagnetics*, (Artech House, Boston, 2003).
- [52] Maslovski, T. A. Morgado, M. G. Silveirinha, C. S. R. Kaipa, and A. B. Yakovlev, Generalized additional boundary conditions for wire media, *New J. Phys.* **12**, 113047 (2010).
- [53] C. S. R. Kaipa, A. B. Yakovlev, S. I. Maslovski, and M. G. Silveirinha, Indefinite dielectric response and all-angle negative refraction in a structure with deeply-subwavelength inclusions, *Phys. Rev. B* **84**, 165135 (2011).

- [54] C. Firestein, A. Shlivinski, and Y. Hadad, Absorption and scattering by a temporally switched lossy layer: Going beyond the Rozanov bound, *Phys. Rev. Appl.* **17**, 014017 (2022).
- [55] D. C. Lay, *Linear Algebra and Its Applications* (Electronic Industry Press, 2018).
- [56] H. A. Haus, P. L. Kelley, and H. J. Zeiger, Generation of Stokes and anti-Stokes radiation in Raman media, *Phys. Rev.* **138**, A960 (1965).
- [57] D. N. Klyshko, *Photons and Nonlinear Optics* (CRC Press, Boca Raton, FL, 1988).